Spectral bidirectional reflectance of Antarctic snow: Measurements and parameterization

Stephen R. Hudson, Stephen G. Warren, Richard E. Brandt, Thomas C. Grenfell, Delphine Six

Spectral bidirectional reflectance of Antarctic snow: Measurements and parameterization

Stephen R. Hudson,[1] Stephen G. Warren,[1] Richard E. Brandt,[1] Thomas C. Grenfell,[1] and Delphine Six[2]

[1] The bidirectional reflectance distribution function (BRDF) of snow was measured from a 32-m tower at Dome C, at latitude 75°S on the East Antarctic Plateau. These measurements were made at 96 solar zenith angles between 51° and 87° and cover wavelengths 350–2400 nm, with 3- to 30-nm resolution, over the full range of viewing geometry. The BRDF at 900 nm had previously been measured at the South Pole; the Dome C measurement at that wavelength is similar. At both locations the natural roughness of the snow surface causes the anisotropy of the BRDF to be less than that of flat snow. The inherent BRDF of the snow is nearly constant in the high-albedo part of the spectrum (350–900 nm), but the angular distribution of reflected radiance becomes more isotropic at the shorter wavelengths because of atmospheric Rayleigh scattering. Parameterizations were developed for the anisotropic reflectance factor using a small number of empirical orthogonal functions. Because the reflectance is more anisotropic at wavelengths at which ice is more absorptive, albedo rather than wavelength is used as a predictor in the near infrared. The parameterizations cover nearly all viewing angles and are applicable to the high parts of the Antarctic Plateau that have small surface roughness and, at viewing zenith angles less than 55°, elsewhere on the plateau, where larger surface roughness affects the BRDF at larger viewing angles. The root-mean-squared error of the parameterized reflectances is between 2% and 4% at wavelengths less than 1400 nm and between 5% and 8% at longer wavelengths.

1. Introduction

[2] The light reflected from a snow surface is diffuse, but not isotropic. This anisotropy is sometimes apparent to the unaided eye and can often be important for geophysical observations and modeling. The angular distribution of reflected light is described by the bidirectional reflectance distribution function (BRDF); here, bidirectional refers to the two directions of interest: that from which the light is coming and that into which the light is being reflected.

[3] Knowledge of a surface's BRDF is a necessary lower boundary condition for accurate modeling of radiative transfer through the atmosphere. Such knowledge is also important for the interpretation of remote-sensing observations. Remote-sensing applications using reflected sunlight generally begin with a measurement of radiance coming from a particular direction. An understanding of the BRDF of the scene being viewed is required either to convert the measured radiance to an upwelling flux, or to normalize the radiance to account for the angular distribution of the reflected light before using it to determine other properties of the scene.

[4] If the radiance measurements are made near the surface, as with many aircraft measurements, then it is the BRDF of the surface that is obtained. For remote sensing using sensors on satellites it is the BRDF of the surface-atmosphere system that is required. Determining this top-of-atmosphere BRDF is difficult because satellites cannot view a scene from all angles in a short period, so the top-of-atmosphere BRDF pattern is typically inferred by combining numerous observations of the same scene type with similar solar zenith angles that were made at different times and span the available range of satellite viewing angles [*Loeb et al.*, 2005]. That method does not require the surface BRDF, but having knowledge of it allows an evaluation of the accuracy of the satellite-derived top-of-atmosphere BRDF.

[5] *Loeb* [1997] and *Masonis and Warren* [2001] used top-of-atmosphere observations of solar radiation reflected from the high surfaces of Antarctica and Greenland to provide estimates of the calibration drift of the sensors for channels 1 and 2 on the Advanced Very High Resolution Radiometer (AVHRR). While their methods do not require a

---

[1]Department of Atmospheric Sciences, University of Washington, Seattle, Washington, USA.
[2]Laboratoire de Glaciologie et Géophysique de l'Environnement, Centre National de la Recherche Scientifique, Université Joseph Fourier, Saint Martin d'Hères, France.

detailed a priori knowledge of the surface BRDF, such knowledge would help improve these techniques.

[6] Many studies have provided estimates of either surface or top-of-atmosphere BRDF for various surface types. Here we present comprehensive measurements of the surface BRDF of Antarctic snow, and parameterizations that allow for the calculation of this BRDF for any viewing geometry, for wavelengths (λ) covering the solar spectrum from 350 to 2400 nm, and for solar zenith angles of 51° to 87°. These parameterizations are strictly applicable to the snow in the vicinity of Dome C, where the measurements were made, but given the homogeneity of the Antarctic Plateau surface, they can probably represent any region of the high plateau having low surface slope.

[7] These measurements and parameterizations complement and extend numerous previous studies of the BRDF of snow. Several recent studies have investigated the BRDF of midlatitude, macroscopically flat snow surfaces [*Leroux et al.*, 1998; *Aoki et al.*, 2000; *Painter and Dozier*, 2004; *Kokhanovsky et al.*, 2005]. Those measurements all include only a few wavelengths or a limited range of solar zenith angles, and they exclude the effects of the macroscale surface roughness found on polar snow. However, they do examine the effect of changing snow type (grain size, grain shape, impurities), which we are unable to do because the snow at Dome C has a relatively stable BRDF since it is always cold, fine-grained, and clean.

[8] Other studies have focused on polar snow. Using a radiometer on an aircraft flying about 600 m above the surface, *Arnold et al.* [2002] measured the BRDF of Arctic scene types, including snow-covered sea ice and tundra, at wavelengths 470–2300 nm with solar zenith angles of about 65° for the snow-covered scenes. *Li and Zhou* [2004] compared modeling results with near-surface measurements of the BRDF of snow-covered late-summer Antarctic sea ice at 4 wavelengths for solar zenith angles of 65° and 85°.

[9] The BRDF of snow on the Antarctic Plateau has been reported by *Kuhn* [1985] and *Warren et al.* [1998]. *Kuhn* [1985] presented spectral measurements from the South Pole at 450, 750, and 1000 nm for a solar zenith angle of 67°, and broadband measurements from Plateau Station for solar zenith angles of 60° and 68°. *Warren et al.* [1998] reported measurements made at South Pole Station at 600, 660, and 900 nm with solar zenith angles from 67° to 89.3°. They examined the effect of the oriented surface roughness features, known as sastrugi, on the measurements and, concluding the effect was minimal at viewing zenith angles less than 50°, provided a parameterization for the BRDF valid for these viewing angles, for dry, fine-grained snow at visible wavelengths, with solar zenith angles in the measured range.

[10] The present work extends the measurements of *Warren et al.* [1998] by covering a broader spectral interval and a wider range of solar zenith angles and by extending the parameterization to longer wavelengths and larger viewing zenith angles. The extension to larger viewing zenith angles was possible because the snow surface at Dome C is smoother than at South Pole, with significantly smaller sastrugi.

[11] In section 2 we introduce the terminology. We then describe the measurements in section 3, then present some

of the results of these measurements and the parameterization in section 4. Section 5 includes some comparisons of the data and parameterization with other data and with some modeling results.

2. Reflectance Terminology

[12] The angles necessary for the discussion of reflectance are illustrated in Figure 1. The solar zenith angle ($\theta_\circ$) and viewing zenith angle (θ_v) are measured from the z-axis. The solar azimuth angle ($\phi_\circ$) and the viewing azimuth angle (ϕ_v) are measured clockwise from north; the viewing azimuth is opposite the direction into which the detected light is traveling.

[13] For most surfaces the BRDF does not depend separately on $\phi_\circ$ and ϕ_v, but instead only on the relative azimuth (ϕ), which we define as the angle measured clockwise from $\phi_\circ$ to ϕ_v. Using this convention, a measurement made with the instrument pointed toward the azimuth of the sun corresponds to $\phi = 0°$, while a measurement made with the instrument pointed 90° to the left of the sun corresponds to $\phi = 270°$.

[14] *Warren et al.* [1998] found this assumption, that ϕ can replace $\phi_\circ$ and ϕ_v, to be invalid at South Pole because of the alignment of the surface roughness features with the prevailing wind direction. However, because our measurements were made at a location with weaker and less directionally constant winds, ϕ appears to be sufficient to describe our observations.

[15] One final geometrical definition is the principal plane, the plane containing the sun, the observer and the z-axis. The BRDF is usually symmetric across the principal plane, an observation we rely on in our data analysis.

[16] The BRDF (ρ, sr^{-1}) is formally defined by *Nicodemus et al.* [1977] as the ratio of the radiance reflected into a particular direction (I_r, W m^{-2} sr^{-1} μm^{-1}), to the incident flux ($F_\circ$, W m^{-2} μm^{-1}), all of which is coming from a single direction:

$$\rho(\theta_\circ, \theta_v, \phi) = \frac{I_r(\theta_\circ, \theta_v, \phi)}{F_\circ(\theta_\circ)}. \quad (1)$$

[17] This definition presents two difficulties for an observer working at the Earth's surface. First, it is impossible to measure reflected sunlight with the incident light all coming from a single direction because of atmospheric scattering. Second, it is difficult to accurately measure the incident flux, especially for large solar zenith angles.

[18] The existence of scattered light means that any observation made with sunlight as the source actually provides the "hemispherical directional reflectance factor," which has the same definition as BRDF except that the incident flux is from the entire hemisphere. Because of the strong wavelength dependence of Rayleigh scattering and the clean air over the Antarctic Plateau, our measurements at wavelengths longer than about 800 nm are essentially of the BRDF of snow, while those at shorter wavelengths, especially below 500 nm, are significantly influenced by diffuse light.

[19] To avoid having to accurately measure the incident flux, we will report our BRDF observations in the form of the anisotropic reflectance factor (R), which was defined by
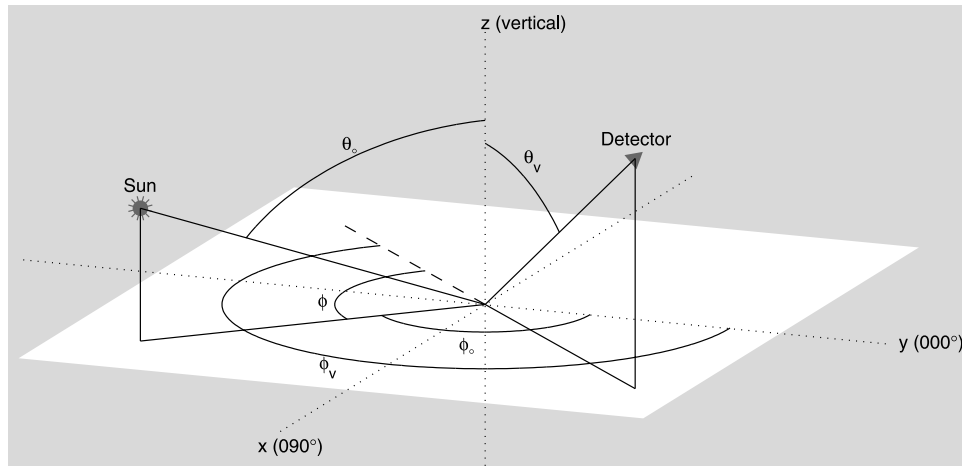
Figure 1. Definition of the solar zenith angle ($\theta_\circ$), the viewing zenith angle (θ_v), the solar azimuth angle ($\phi_\circ$), the viewing azimuth angle (ϕ_v), and the relative azimuth angle (ϕ).

Suttles et al. [1988] as π times the ratio of radiance reflected into a particular direction, to the reflected flux:

$$R(\theta_\circ, \theta_v, \phi) = \frac{\pi I_r(\theta_\circ, \theta_v, \phi)}{\int_0^{2\pi} \int_0^{\pi/2} I_r(\theta_\circ, \theta_v, \phi) \cos\theta_v \sin\theta_v \mathrm{d}\theta_v \mathrm{d}\phi}. \quad (2)$$

Multiplying by π sr makes this function nondimensional and ensures that its average value over the upward hemisphere, weighted by its contribution to the upward flux (proportional to $\cos\theta_v$), is unity:

$$\frac{1}{\pi} \int_0^{2\pi} \int_0^{\frac{\pi}{2}} R(\theta_\circ, \theta_v, \phi) \cos\theta_v \sin\theta_v \mathrm{d}\theta_v \mathrm{d}\phi = 1. \quad (3)$$

An isotropic (Lambertian) reflector has $R = 1$ at all angles.

[20] The spectral albedo (α) is the ratio of reflected to incident flux as a function of wavelength, and its values for snow on the Antarctic Plateau have been reported before [*Grenfell et al.*, 1994], and we also measured similar values near our BRDF site. The albedo can be derived from the BRDF as

$$\alpha(\theta_\circ) = \int_0^{2\pi} \int_0^{\frac{\pi}{2}} \rho(\theta_\circ, \theta_v, \phi) \cos\theta_v \sin\theta_v \mathrm{d}\theta_v \mathrm{d}\phi, \quad (4)$$

which illustrates that R and ρ differ by a factor of $\frac{\pi}{\alpha}$:

$$R(\theta_\circ, \theta_v, \phi) = \frac{\pi}{\alpha} \rho(\theta_\circ, \theta_v, \phi). \quad (5)$$

3. Measurements

3.1. Location

[21] All measurements reported in this paper were made at Dome C (75°06′S, 123°18′E, 3200 m MSL) during the summers of 2003–2004 and 2004–2005. This site was chosen because it is in the low-latitude part of the plateau, 15° from the pole, which allows measurements at a wide range of solar zenith angles each day, and because it is near

a local maximum in ice sheet elevation, which means winds there are generally lighter and less directionally constant than at other plateau sites because the surface slope at Dome C is extremely small. The lighter and more variable winds minimize the effect of surface roughness on the observations by creating smaller and less aligned sastrugi. The latitude of 75° is seen frequently by most polar-orbiting satellites.

[22] The observations were made from atop a 32-m tower to ensure that the instrument's footprint was large enough to include a representative sample of the rough snow surface. A footprint that is too small may be dominated by a single, unrepresentative surface feature. The instrument's field of view has a diameter of 15°, and measurements were centered on viewing zenith angles of 22.5°, 37.5°, 52.5°, 67.5°, and 82.5°. The areas of the footprints at the first four angles were about 70, 110, 260, and 1170 m² ; the footprint at 82.5° extends to the horizon. Even the smallest of these footprints should contain multiple sastrugi.

[23] The French and Italian Antarctic programs have been jointly operating a small summer research camp at Dome C since 1996. The last few years have seen the construction of a new, year-round base, which was first occupied during the winter of 2005. The tower on which we operated was erected in the summer of 2002–2003 in a previously undisturbed area. It is situated about 900 m WNW of the construction site for the year-round base, 1300 m WNW of the summer camp, and 1700 m WNW of the runway. Travel was forbidden inside a large region, providing us with an undisturbed snow surface over 255° of azimuth, from $\phi_v = 142.5°$ clockwise to $\phi_v = 37.5°$. By the time we began BRDF measurements, in December 2003, all of the surface disturbances caused by the tower installation had been erased by 11 months of blowing and falling snow. Snow samples collected near our site had soot concentrations around 3 ng of carbon per gram of snow (ng g^{-1}) in the upper 0.2 m of snow (that which had fallen since the tower was installed), and about 1 ng g^{-1} in deeper snow [*Warren et al.*, 2006]. *Warren and Clarke* [1990] suggested a soot concentration of 3 ng g^{-1} would reduce the albedo at the most sensitive wavelength by less than 0.004, indicating
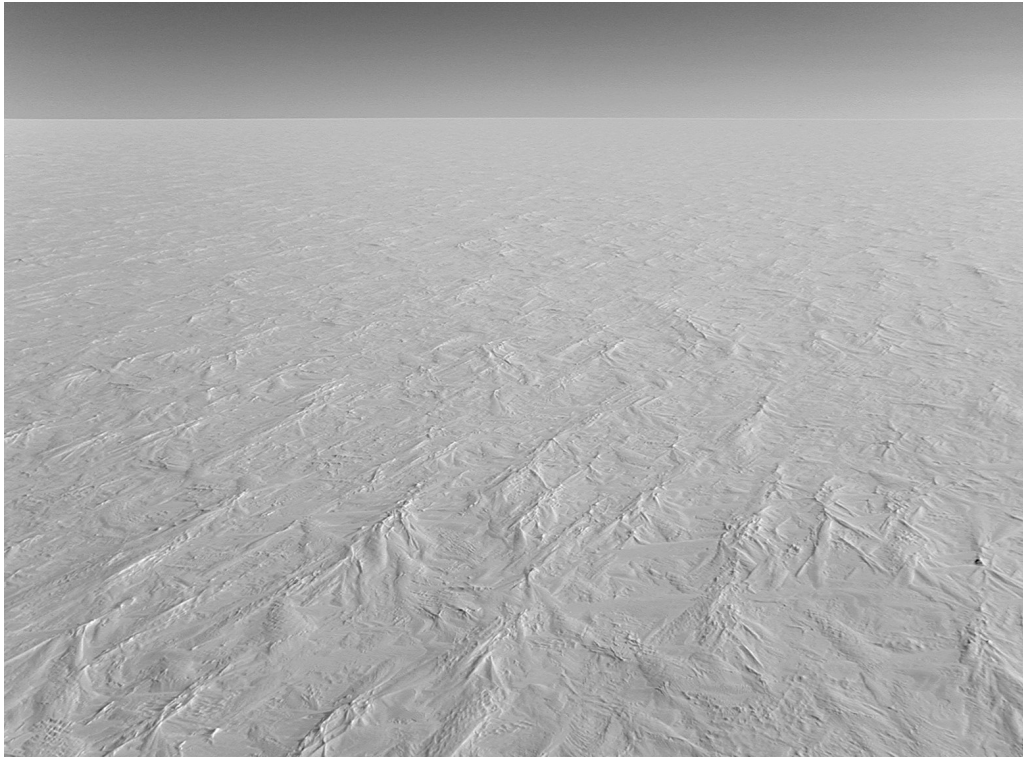
Figure 2. A photograph looking west from the top of the 32-m tower from which the BRDF measurements were made. The sun is in the north.

that this level of contamination produces no significant impact on our observations.

[24] Figure 2 shows the appearance of the snow surface to the west of the tower. A theodolite and leveling rod were used on several days to measure the surface elevation every 20 or 50 cm along numerous 20- to 35-m lines in areas just outside our measurement domain. The standard deviation of these data was 2.3 cm, and the highest sastrugi were only 6 to 8 cm above the mean surface.

3.2. Equipment and Experimental Design

[25] All radiance measurements were made using a Field-Spec Pro JR spectroradiometer manufactured by Analytical Spectral Devices, Inc. (hereinafter referred to as ASD). The ASD records the radiance every 1 nm from 350 to 2500 nm, with 3- to 30-nm spectral resolution (full width at half-maximum). More details about the ASD are given by *Kindel et al.* [2001].

[26] The fiber optic input cable to the ASD was mounted in a baffle, limiting its field of view to a 15° cone. This baffle was then mounted on a goniometer, which allowed for accurate pointing in both the zenith and azimuth. The pointing of the goniometer was performed manually. The ASD and the laptop computer with which it interfaced were both kept at the top of the 32-m tower inside heated boxes.

[27] Each observation sequence involved recording the radiance coming from 85 different locations on the snow surface. Each of the 85 recorded measurements was an average of 10 of the ASD's spectral scans; each 10-scan average took less than 3 s to complete. An entire observation sequence, including positioning the goniometer to point

at each location and driving the computer, took between 10 and 15 min to complete.

3.3. Generation of Anisotropic Reflectance Patterns

[28] During each observation, measurements were made every 15° in both θ_v (22.5°, 37.5°, 52.5°, 67.5°, and 82.5°) and ϕ_v (150°, 165°, ..., 345°, 0°, 15°, and 30°). These points represent the locations that would be viewed by an infinitesimal field of view; the intersection of our 15° conical field of view with the surface creates an ellipse, with the two foci along a line extending in the direction of ϕ_v, from below the goniometer's location.

[29] For planning purposes, observation sequences were centered on times when ϕ_o was a multiple of 15°. The local standard times at which the desired solar geometry would occur on each day were calculated using a program adapted by Warren Wiscombe from *Michalsky* [1988].

[30] To ensure both that the incoming solar flux did not change significantly during an observation, and that no measurements were affected by shadows, observations were made only when the sky either was clear or contained very few clouds, all of which were thin and within a few degrees of the horizon.

[31] Because the snow to the east of the tower was disturbed by buildings and foot and vehicle traffic, radiances could be measured from only about two thirds of the viewing azimuths during each observation sequence. In order to generate anisotropic reflectance functions, reflected radiances must be available from all azimuths to carry out the integral in the denominator of equation (2). We chose one of the following two methods to complete each

pattern, depending on the location of the sun during the measurements.

[32] For those observations that contain measurements at both $\phi = 0°$ and $\phi = 180°$, and therefore contain measurements at all azimuths on one side of the principal plane, we relied on the observation that the BRDF is approximately symmetric across this plane to allow us to complete the patterns by reflecting measurements across the principal plane (e.g., we set $R(\theta_\circ, \theta_v, \phi = 45°) = R(\theta_\circ, \theta_v, \phi = 315°)$ if we had measurements from $\phi = 180°$ clockwise to $\phi = 0°$). Our available viewing geometry meant that this method was applied to observations with $\phi_\circ$ within $30°$ of $0°$ or $180°$, which were those made during the period between about two hours before and after noon and midnight local time.

[33] To complete patterns using observations made at other times, two separate observations, with equal solar zenith angles, but different solar azimuth angles, were combined. Observations made within about 36 hours of each other, with equal values of $|180° - \phi_\circ|$ have approximately equal solar zenith angles and could be combined. This method requires R to be a function only of the relative azimuth, and our measurements showed this to be a reasonable assertion. To make a complete pattern, measurements at each of the 24 relative azimuths must exist in at least one of the two observations. This was true of the correct combinations of observations made between about two hours before and after 0600 and 1800 local time.

[34] When this method of stitching two partial patterns together is used, a scale factor must be applied to one of the patterns to account for small changes in atmospheric conditions and any changes in the instrument response. All observations that were stitched together contained at least 10 angles at which measurements were made in both observations. Ratios of these overlapping measurements provided numerous possible scale factors, from which one was chosen using the method described by *Warren et al.* [1998]. Various methods to determine a single scale factor from the numerous overlapping measurements, including taking the mean or median of the possible factors and the method used by *Warren et al.* [1998], produced patterns with insignificant differences.

[35] Once a complete pattern was available, the solar geometry was determined for the time of each of the 85 individual measurements. Each radiance measurement was then divided by the cosine of the solar zenith angle at the time of that measurement to account for variations in reflected radiance caused by the small variation of $\theta_\circ$ during the time required for the complete observation. For a few of the measured directions, the field of view contains part of the tower's shadow. We therefore discarded the measurements at ($\phi = 180°$, $\theta_v < \theta_\circ + 7.5°$) and ($\phi = 165°$ and $\phi = 195°$, $\theta_v = 22.5°$) and replaced them with estimates determined by fitting a cubic spline to data from the neighboring backscattered azimuths at the same viewing zenith. No measurements were made closer to nadir than $22.5°$. Radiances at all azimuths at $\theta_v = 7.5°$ were therefore set to the median of the measurements at $\theta_v = 22.5°$. The data were then interpolated to a fixed angular grid: every $7.5°$ in ϕ, beginning at $0°$, and every $15°$ in θ_v, beginning at $7.5°$. For the interpolation of the values in the shadow region and for the gridding process, the measurements were placed at their actual relative azimuth, as calculated for the time of each

measurement, rather than at their nominal relative azimuths; the two differ slightly because of the roughly $3°$ to $4°$ change in $\phi_\circ$ during the observation sequence.

[36] At this point we have a complete and consistent set of reflected radiance measurements. These are then normalized using equation (2), providing the anisotropic reflectance functions that are used in the rest of this paper.

3.4. Experimental Uncertainties

[37] *Warren et al.* [1998] discussed five major factors that affect the BRDF of snow: single-scattering phase function, solar zenith angle, snow grain size, absorption coefficient of ice, and surface roughness. Of these, only the solar zenith angle changes appreciably in the time required for an observation sequence. The microscale properties of the snow are relatively homogeneous around Dome C, but spatial variations of the surface roughness features can affect our observations.

[38] Macroscopic surface roughness features can alter the BRDF of a surface. In general they will cause an observer facing the sun to see shadowed or shaded surfaces, thus reducing the magnitude of the forward reflectance peak. The roughness also increases the amount of backscatter by effectively reducing the solar zenith angle on roughness elements. The dimensions and orientation of the features determine how large this effect is.

[39] Observation of the surface roughness features was not viewed as something to avoid because they make our data appropriate for use on the high Antarctic Plateau. However, the surface roughness can introduce uncertainties into our observations in three ways: its effect may vary depending on the area of the observation footprint on the surface; the roughness can vary within our observation domain, producing different effects at different viewing angles; the roughness elements may have a preferred orientation, causing asymmetries across the principal plane.

[40] As discussed in section 3.1, the observations were made from the top of a tower to provide a large enough footprint to include a representative sample of surface roughness elements. Still, the area of the footprint does increase significantly as the viewing zenith angle increases. This increasing spatial averaging may affect our observations. We expect that this effect is likely to be small since the surface roughness mostly affects the BRDF at the largest viewing zenith angles [*Warren et al.*, 1998], both of which have extremely large footprints, however, a rigorous assessment of this effect would require the use of a three-dimensional Monte Carlo radiative transfer model with the snow surface roughness features realistically described. Such modeling has not been carried out, and is beyond the scope of this paper. The potential effect of variations in R due to different amounts of spatial averaging should also be considered by those using surface and satellite observations together.

[41] The measurements at each viewing angle observe different areas of the surface. This means there could be differences in the observed radiance field that are due to the observation of areas with different surface roughness features. Given the small size (relative to the footprint area) and random spatial distribution of the surface features seen in Figure 2, it is unlikely that any one footprint will fall on a

truly unrepresentative area, especially at the larger viewing zenith angles, where the roughness has the greatest effect.

[42] If the surface features have a preferred orientation, they can cause asymmetries across the principal plane, and this effect will vary depending on the orientation of the roughness features relative to the solar azimuth [*Warren et al.*, 1998, Figure 5]. Since our methods of generating complete reflectance patterns assume that the reflectance is symmetric across the principal plane and that it is affected only by the relative azimuth angle, these roughness features may cause variations that we do not account for in our results.

[43] The small size and variable orientation of the surface features at Dome C minimize these sources of uncertainty. To estimate the magnitude of the error introduced into our analyzed patterns due to our assumption of symmetry across the principal plane, we calculated, for all observations used in the analyses, the relative difference between radiance measurements made during the same observation, with the same θ_v and with $|\phi|$ $(-180° < \phi \leq 180°)$ within 4° of each other. These calculations do not isolate the effect of the assumption of symmetry; they will be affected by other sources of noise as well. At $\lambda \leq 1400$ nm the difference between such measurement pairs, for all θ_o, is generally less than 5%, and at longer wavelengths it is generally less than 10%. The largest differences occur at wavelengths with the lowest albedo, where the noise in the observations is greatest. These differences increase with θ_o but show no systematic variation with ϕ or θ_v. If these differences were entirely due to asymmetry across the principal plane caused by surface roughness then, from Figure 6 of *Warren et al.* [1998], we would expect the differences to increase with θ_v and to decrease with ϕ (away from the forward scattering direction). That they do not suggests that they are influenced by other sources of noise as well.

[44] Aside from factors that actually affect the BRDF of snow, other effects can introduce error into our measurements. These include errors introduced by variations in the amount of incoming flux, with either time or space, and those caused by instruments or observation methods.

[45] During the field seasons we made BRDF observations only when it appeared they would be unaffected by clouds. It is possible that some errors will be introduced into the observations as a result of variations in downwelling fluxes due to subvisible clouds or boundary layer ice crystals (diamond dust), a phenomenon too common to avoid completely. Diamond dust was present during about 25% of our observations. Variations in incoming flux due to changing solar elevation should be largely accounted for by our data processing.

[46] Tests showed that the repeatability of radiance measurements made with the ASD was within ±2% over a 20-min period, enough time for a complete set of measurements. Because R is normalized by the reflected flux, an absolute calibration was not necessary.

[47] Small errors may have been introduced through inaccurate pointing of the goniometer. The goniometer was aligned in azimuth with reference to the shadow of the tower together with the equation of time for that day; it was leveled with a manufacturer-installed bubble level on its base. We estimate that our installation and pointing were accurate to within ±2° in both zenith and azimuth.

[48] It is impossible to estimate with a high degree of confidence the combined uncertainty from these numerous potential sources. Comparisons of separate analyzed patterns with solar zenith angles that differ by less than 1° suggest that the overall uncertainty is within ±3% at $\lambda <$ 1400 nm with small θ_o ($\lesssim 60°$), ±8% at longer wavelengths with small θ_o, ±6% at $\lambda < 1400$ nm with large θ_o($\gtrsim 70°$), and ±15% at longer wavelengths with large θ_o. In general, uncertainty is larger at wavelengths with low albedos and in observations made with large solar zenith angles. Both of these situations reduce the amount of light reaching the detector, which may cause a lower signal-to-noise ratio, but probably more important is that both also significantly increase the anisotropy of the snow BRDF and its sensitivity to variations in grain radius. Uncertainty is also larger at longer wavelengths because of the increased anisotropy of the reflected radiation due to the lack of diffuse downwelling radiation. Increased anisotropy enhances the effect of small pointing errors.

4. Results

4.1. Observations

[49] A few examples of the patterns of R resulting from our data analysis are shown in Figures 3 and 4. These polar plots show contours of the value of R as a function of θ_v (distance from center) and ϕ (angle clockwise from top) for various wavelengths and solar zenith angles.

[50] Figure 3 shows examples of R measured at two wavelengths with contrasting albedos: 600 nm ($\alpha \approx 1.0$) and 1800 nm ($\alpha \approx 0.3$), for high, middle, and low solar elevations. These observations will be compared later with results of the parameterizations. Figure 4 shows R measured at 2000 nm (very low albedo; $\alpha < 0.1$) for high and low solar elevations.

[51] Figures 3 and 4 illustrate the two main features of the data: the snow is brightest when viewed near the horizon, in the direction of the solar azimuth, darkest when viewed near nadir, opposite the solar azimuth; and this anisotropy increases with increasing solar zenith angle and decreases with increasing albedo. Figure 3 (top left) is typical of the observations that are nearly isotropic.

[52] During the two summers of observations we collected data to create 96 complete patterns of R, at solar zenith angles from 51.6° to 86.6°. Subsequent analysis revealed that the data at $\lambda > 2400$ nm were unreliable because of a low signal-to-noise ratio, so the analysis covers wavelengths from 350 to 2400 nm. Given the volume of data collected, we cannot present them all here, so those in Figures 3 and 4 were chosen as representative examples. More of the data can be viewed in the auxiliary material[1] published online along with this paper and available on our website (http://www.atmos.washington.edu/~sgwgroup/DC/brdfPaper.html). The values of R at the gridded angles are available there at any of the 96 measured solar zenith angles at 25-nm intervals for wavelengths between 350 and 2400 nm.

4.2. Parameterization

[53] With such a large set of data available, we hoped to be able to develop and present a parameterization that could

---
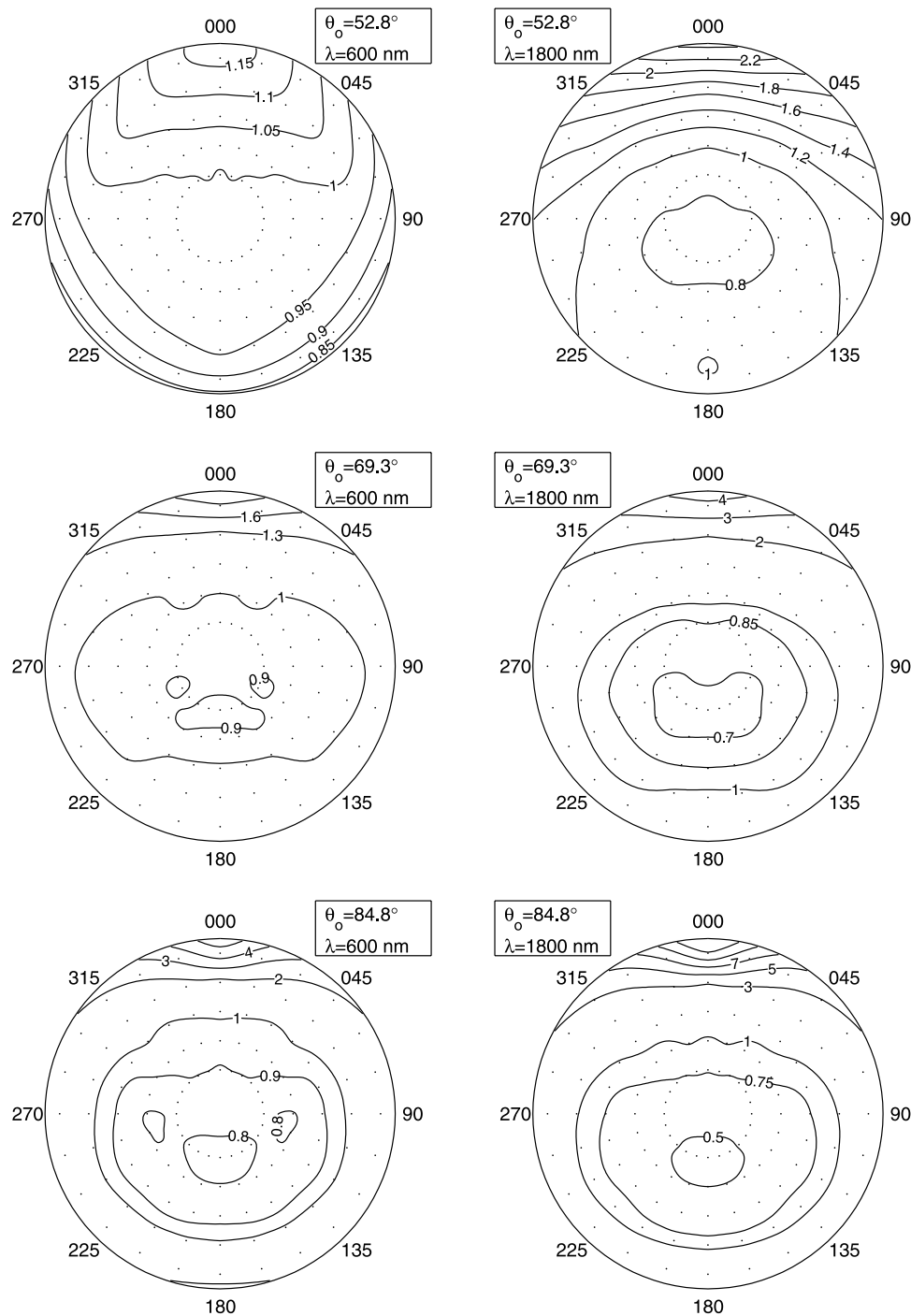
Figure 3. Polar contour plots of the anisotropic reflectance factor (*R*) of snow at Dome C measured under three different solar zenith angles at two different wavelengths (λ). Dots are placed every 15° in both viewing zenith angle, starting at 22.5°, and relative azimuth angle, starting at 0°, which indicates light coming from the azimuth containing the sun. The contour interval for *R* < 1 sometimes differs from that for *R* > 1.

be used to predict *R* for any solar zenith angle and wavelength within the range we observed. The data proved too variable to allow for a single parameterization to accurately describe them all. However, by separating the data into a few groups, on the basis of wavelength or albedo, solar zenith angle, and, sometimes, viewing zenith angle, it was possible to develop multiple parameterizations

that fit the data with reasonable accuracy. These separate parameterizations cover most of the range of wavelengths and solar zenith angles observed, but some of the most extremely anisotropic cases, those with very low albedo, are not covered.

[54] In this section we will first show how the data vary with wavelength, albedo, and solar zenith angle, and discuss
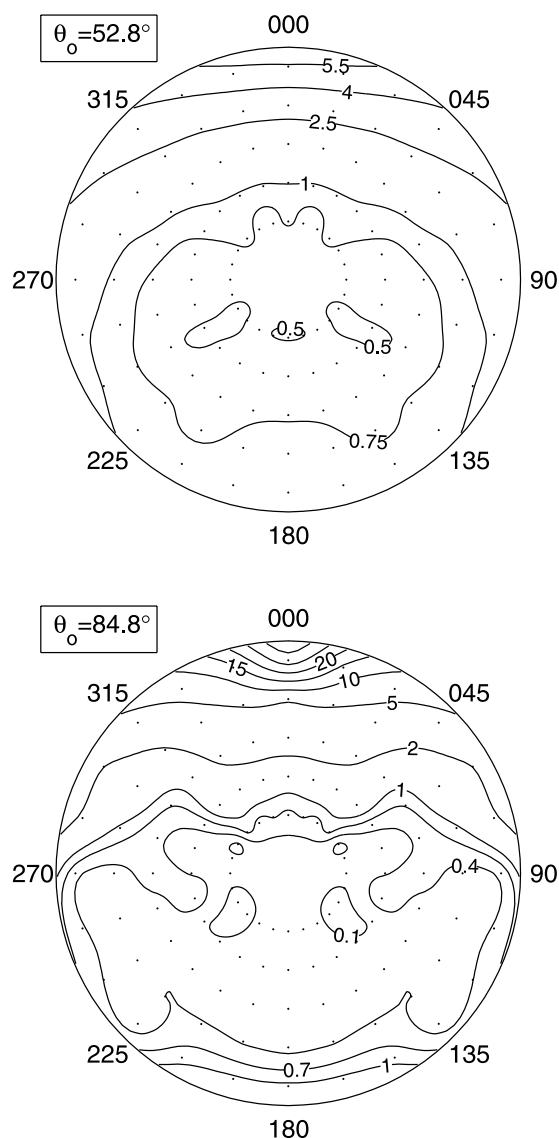
Figure 4. Polar contour plots of R measured at a wavelength of 2000 nm under two different solar zenith angles. Note that the contour interval is not constant.

why the parameterizations use the predictors they do and how we divided the data. After that we will explain the functions used in the parameterizations, and how these parameterizations were developed. Finally we show selected results from the parameterizations.

4.2.1. Variation of R With $\theta_\circ$, λ, and α

[55] The values of R at ($\theta_v = 82.5°$, $\phi = 0°$) as a function of wavelength are shown in Figure 5 for observations at three different solar zenith angles. We present R at the forward reflectance peak because it is a good indication of the anisotropy of the overall pattern. We will abbreviate $R(\theta_v = 82.5°, \phi = 0°)$ as R_f. From Figure 5 we can see that the anisotropy does not increase monotonically with wavelength. At wavelengths longer than about 1000 nm the anisotropy varies with wavelength in a way that may seem erratic.

[56] One feature in Figure 5 that may seem unusual is the crossing of the curves for the two larger solar zenith angles

at $\lambda = 375$ nm. This feature is the result of the varying amount of diffuse light incident on the snow. Diffuse incident flux acts to reduce the anisotropy of the reflected light: if the incident flux were isotropic, then there would be no forward direction into which light could be preferentially scattered. As the sun descends toward the horizon, the fraction of the incident flux that has been scattered out of the direct beam increases. This effect is larger at shorter wavelengths, where Rayleigh scattering is most effective. This combination is enough, in the ultraviolet region, to overcome the usual pattern of increasing anisotropy with solar zenith angle.

[57] Of the five factors listed in section 3.4 that affect the BRDF of snow, the single-scattering phase function and the absorption coefficient of ice both vary with wavelength. For a given grain radius and solar zenith angle, the albedo of the snow is largely determined by these two factors, suggesting that R, under direct-beam illumination, should be the same at any wavelengths at which snow has the same albedo.

[58] The albedo of the snow at Dome C was measured one evening when clouds were thick enough to fully obscure the solar disk so that all incident flux was diffuse. Having only diffuse light incident on the snow greatly reduces the magnitude of errors that are introduced by small deviations from level of either the surface or the instrument. Figure 6 shows the albedo measured that evening, as a function of wavelength. The measured albedo at Dome C closely resembles that measured at the South Pole [*Grenfell et al.*, 1994]. Comparing Figures 5 and 6 supports the suggestion that albedo may be a better predictor of R than wavelength since the maxima of R_f are located near the minima of α.

[59] A plot of R_f versus α, shown in Figure 7, confirms that this relationship is much more systematic than that shown in Figure 5. Figure 7 was created by plotting the values of R_f observed every 25 nm during three different observations (corresponding to the three solar zenith angles) versus the albedo from Figure 6 at that wavelength, so it shows the clear-sky R_f versus the diffuse (overcast) albedo. This plot shows a very good power-law relationship between the anisotropy of the reflected light and the albedo of the snow at albedos between about 0.15 and 0.95. The failure of the relationship at low albedos may result from noise due to the very small amounts of reflected light at these wavelengths, or it may represent variability caused by some other factor we have not considered here. At high albedos the relationship fails because these albedos occur in the visible and ultraviolet, where Rayleigh scattering causes a significant amount of diffuse downwelling radiation. A similar approach using clear-sky albedo might work as well as or better than using the diffuse albedo, but would require using a different spectral albedo for each solar zenith angle. However, the sorting of wavelengths according to their albedos will be nearly the same for all zenith angles, judging from Figure 11a of *Wiscombe and Warren* [1980], so Figure 7 would likely remain unchanged.

[60] We considered the imaginary index of refraction of ice (m_{im}) as a predictor, rather than albedo, but chose to use albedo for two reasons. A plot, similar to Figure 7, of R_f versus m_{im} (not shown) showed that this relationship did not follow a simple functional form. Also, the albedo incorporates the variation of the single-scattering phase function
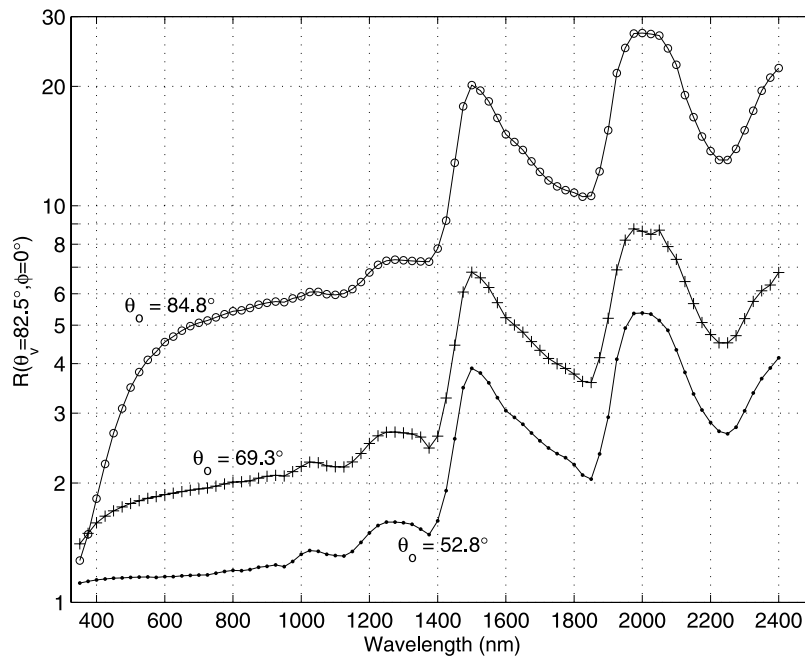
Figure 5. Values of R measured at the forward reflectance peak, as a function of wavelength, for three different solar zenith angles.

with λ, and will allow the parameterization to be used for snow with different grain sizes than the snow at Dome C. If a user of the parameterization wishes to apply it to snow with larger grains, and therefore lower albedo in the near-infrared, the different grain size can be accounted for by using an estimate of the albedo of the snow of interest rather than the measured albedo of the snow at Dome C (Figure 6).

[61] Figure 7 shows that wavelengths with the same albedo have the same forward peak, but do their BRDFs also agree at other angles? To answer this, complete angular patterns of R were compared at wavelengths with the same albedo. The patterns observed at 1450 nm and 2250 nm ($\alpha = 0.187$ at both wavelengths) show maximum differences of 8% with $\theta_\circ = 60°$ and 12% with $\theta_\circ = 80°$, and both differ
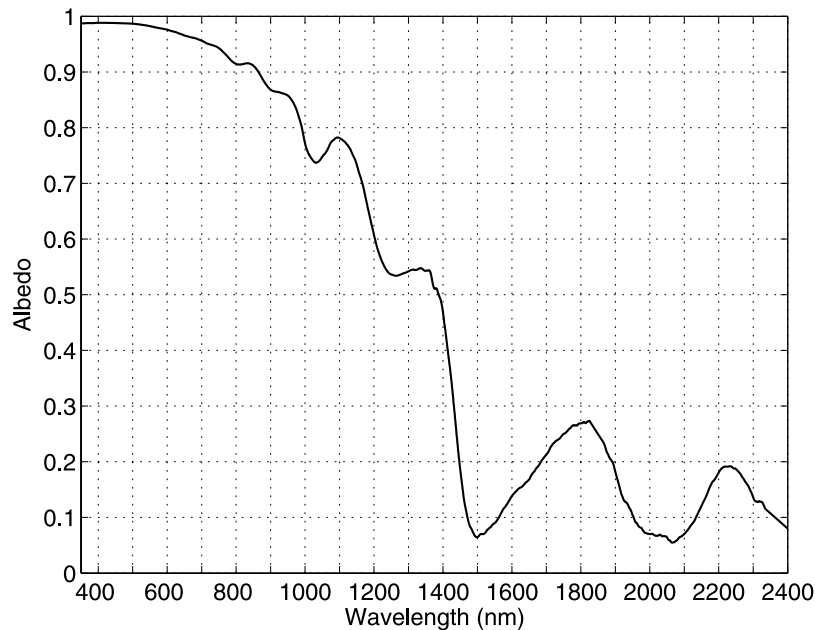
Figure 6. Spectral albedo of the snow surface at Dome C, measured between 2300 and 2330 LST 30 December 2004 under an overcast sky with the direct solar beam fully obscured. Five observations were averaged, and this average was then smoothed using an 11-nm running mean at $\lambda \leq$ 1825 nm and a 101-nm running mean at larger wavelengths, where extremely low fluxes resulted in a low signal-to-noise ratio.
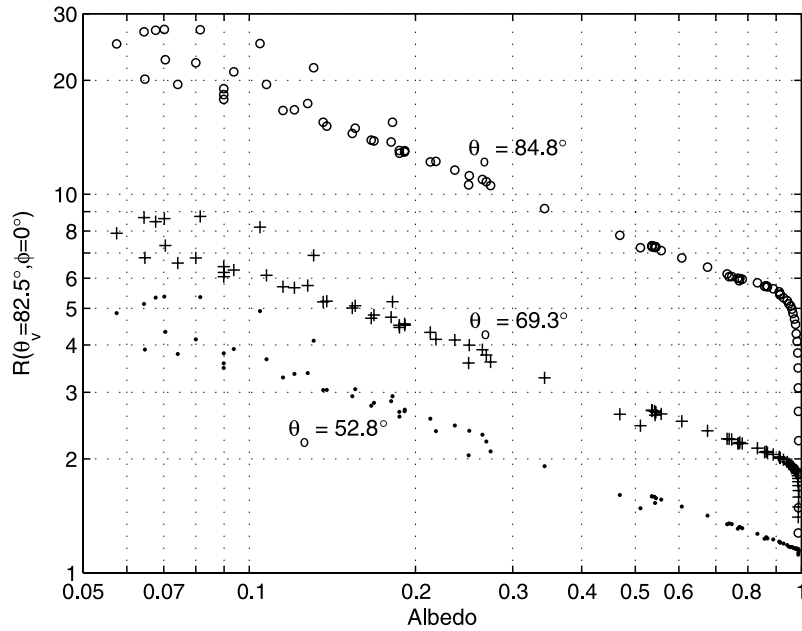
Figure 7. Values of R measured at the forward reflectance peak, as a function of albedo, for three different solar zenith angles.

by less than 6% at nearly all viewing angles. Similar small differences were found between the observed patterns at other pairs of wavelengths with equal albedos. In contrast to these small differences, observed patterns at the nearby wavelengths of 1400 nm ($\alpha = 0.47$) and 1450 nm ($\alpha = 0.19$) differ by up to 60%.

[62] On the basis of results shown above, we chose to consider three wavelength regions. At short wavelengths, 350 to 950 nm, where Rayleigh scattering may affect our measurements and albedo varies smoothly with wavelength, we chose to use wavelength as a predictor in the parameterization. At longer wavelengths, we chose to use the albedo shown in Figure 6 as the predictor. We split the longer-wavelength region into one from 950 to 1400 nm, where the albedo is intermediate, and another from 1450 to 2400 nm, where the albedo is low. We further limited this latter region by excluding wavelengths at which $\alpha < 0.15$. This last restriction means the regions near 1500, 2000, and 2400 nm (e.g., Figure 4) are not included in the parameterizations. Data between 1400 and 1450 nm were also not included because α varies so rapidly with wavelength in this region. Data at wavelengths not included in the parameterizations are available with the auxiliary material online.

[63] The other necessary predictor in the parameterizations is the solar zenith angle. The variation of R_f with $\theta_\circ$ is shown for several wavelengths in Figure 8. Figure 8 shows that at most wavelengths the anisotropy is nearly independent of $\theta_\circ$ for $\theta_\circ \lesssim 60°$, then increases with $\theta_\circ$, at an increasing rate as $\theta_\circ$ increases. Again, the relationship is different at short wavelengths ($\lambda = 375$ nm), where the great reduction in the direct/diffuse ratio as the sun approaches the horizon leads to decreased anisotropy.

[64] Separate parameterizations were developed for high and low sun. The primary parameterization for each of the three wavelength regions is for $\theta_\circ \leq 75°$. Parameterizations for $\theta_\circ \geq 70°$ were developed for the two shorter-wavelength

regions; an accurate parameterization for the low-sun data at long wavelengths could not be developed because of their more extreme anisotropy, seen in Figure 3 (bottom right). The high- and low-sun parameterizations overlap for $70° \leq \theta_\circ \leq 75°$. This was done so that the low-sun parameterizations would be valid through the gap in our data between $75°$ and $79°$ (seen in Figure 8). In the region where both parameterizations are valid, the one for $\theta_\circ \leq 75°$ works better.

[65] There was one final separation of the data necessary to develop accurate parameterizations. The long-wavelength data were separated into large and small viewing zenith angles at $\theta_v = 52.5°$; this angle is included in both. These two parameterizations produce nearly equal results at $\theta_v = 52.5°$ (the RMSE at $52.5°$ is 5.8% for the $\theta_v \geq 52.5°$ parameterization and 6.1% for the $\theta_v \leq 52.5°$ parameterization).

[66] There are six groups of data to be parameterized, summarized in the first five columns of Table 1; the last two columns of the table will be discussed later.

4.2.2. Parameterization Development

[67] Rather than use predefined functional forms to describe the data, such as Fourier series, which would require many terms to capture the more extreme anisotropy that exists in some of the data, we chose to use the empirical orthogonal functions (EOFs) of the data. The EOFs are a set of orthonormal functions determined by performing a singular value decomposition of the data matrix. These functions are ordered such that the first one is the pattern that describes a larger fraction of the variance in the data than any other EOF, and the second is the function, orthogonal to the first that can describe more of the remaining variance than any other, and so on. The advantage of EOF analysis is that most of the significant variance in a data set can be represented with just the first few EOFs, making them ideal for use in our parameterizations.
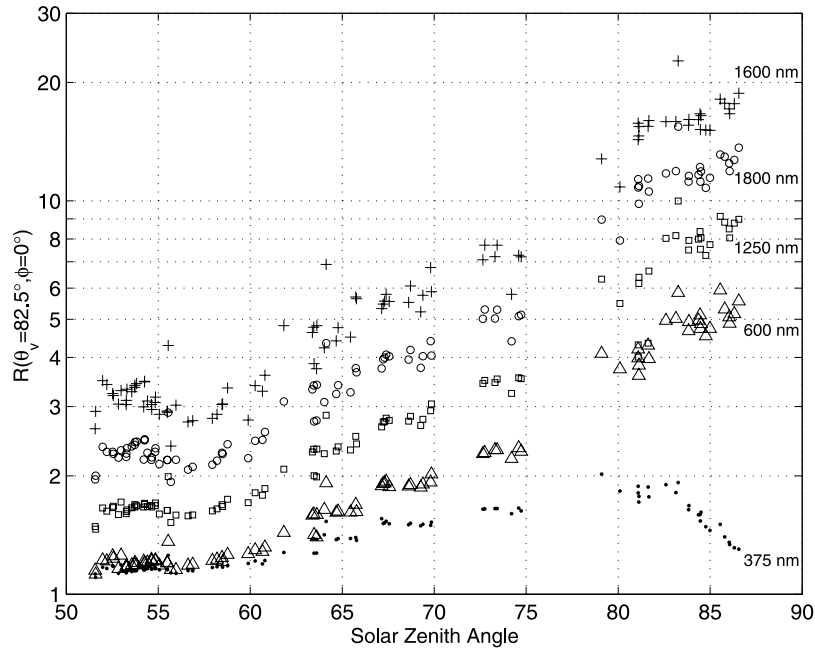
Figure 8.   Values of R measured at the forward reflectance peak, as a function of solar zenith angle, for five wavelengths: 375 nm, dots; 600 nm, triangles; 1250 nm, squares; 1600 nm, crosses; and 1800 nm, circles.

[68] Here we will work through a specific example of how this procedure was used to develop a parameterization. We use the subset of data that includes $\lambda \leq 950$ nm, $\theta_\circ \leq 75°$. This subset includes 71 observations at different solar zenith angles. For the development of the parameterizations, data at wavelengths that are integer multiples of 25 nm were used, meaning that this subset includes patterns of R at 25 wavelengths (350, 375, 400, . . . , 950 nm). So, there are $71 \times 25 = 1775$ different patterns included in the development of this parameterization. Each pattern contains the values of R gridded at 288 angular locations (6 viewing zenith angles and 48 viewing azimuth angles). Combining these numbers gives us a data matrix ($\mathbf{R}$) that has 1775 columns and 288 rows; each column contains all of the gridded values of R for one pattern, in some specified order, which is constant across all columns.

[69] A technical-computing software package (Matlab) was used to compute the singular value decomposition of the data matrix minus one, decomposing the data into three matrices such that:

$$\mathbf{R} = \mathbf{1} + \mathbf{U\Sigma V}^{\mathrm{T}} \qquad (6)$$

where $\mathbf{1}$ is a 288×1775 matrix of ones. The EOFs are contained in the columns of $\mathbf{U}$, a 288×288 matrix (there are 288 rows because the EOFs are defined at the same grid points as the data, and there are 288 columns because there are as many spatial EOFs as there are spatial grid points). The first and second EOFs (the first and second columns of $\mathbf{U}$) are contoured in Figure 9.

[70] The first column of $\mathbf{V}$, a 1775×288 matrix, contains the coefficients that multiply the first EOF to make each of the 1775 patterns. The second column of $\mathbf{V}$ are the coefficients that multiply the second EOF, and so on. The third matrix in equation (6), $\mathbf{\Sigma}$, is a 288×288 matrix with positive scale factors on its diagonal, and zeros elsewhere. The values on the diagonal of $\mathbf{\Sigma}$ are in decreasing order, and are related to the amount of variance represented by each EOF.

[71] While the singular value decomposition initially increases the number of values needed to describe the data from $288 \times 1775 = 511,200$ to $288 \times 288 + 288 + 1775 \times 288 = 594,432$ (ignoring the off-diagonal elements of $\mathbf{\Sigma}$), the power of the decomposition comes from the ability to recover the important aspects of the data with just the first

Table 1.   Summary of the Data Included in and the Root-Mean-Squared Relative Errors of the Six Parameterizations[a]

| Parameterization | Data Included in Parameterizations | | | | RMS Error | |
	λ, nm	$\theta_\circ$	α	θ_v	All θ_v	$\theta_v \leq 52.5°$
A	350–950	51.6°–75°	n/a	0°–82.5°	2.3%	1.9%
B	350–950	70°–86.6°	n/a	0°–82.5°	3.7%	3.0%
C	950–1400	51.6°–75°	0.47–0.86	0°–82.5°	3.5%	2.7%
D	950–1400	70°–86.6°	0.47–0.86	0°–82.5°	4.1%	3.7%
E	1450–2400	51.6°–75°	0.15–0.28	0°–52.5°	5.6%	5.6%
F	1450–2400	51.6°–75°	0.15–0.28	52.5°–82.5°	7.9%	n/a

[a]The errors given for parameterizations E and F in the "All θ_v" column are for all angles included in the parameterization.
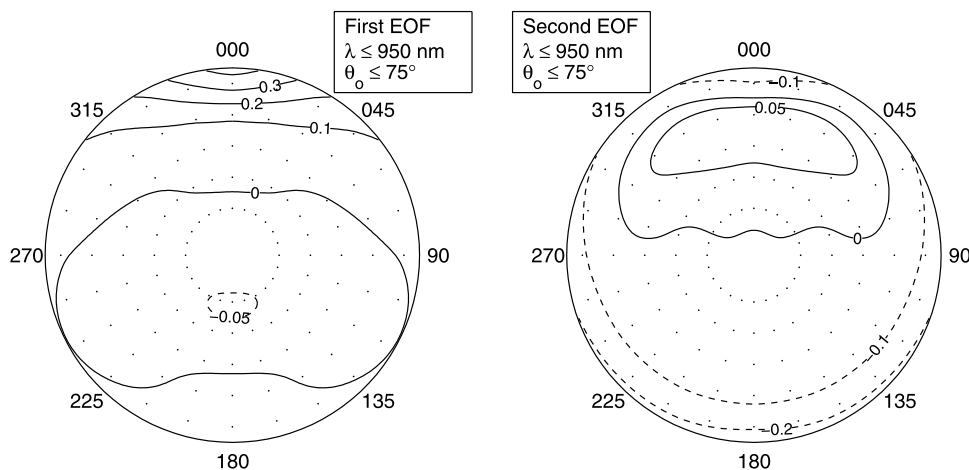
Figure 9. Polar contour plots of the first and second EOFs used in parameterization A. Contours of negative values are dashed.

few columns of **U**, **Σ**, and **V**, thus greatly reducing the volume of data. In this case, the first two columns ($288 \times 2 + 2 + 1775 \times 2 = 4128$ values) contain enough information to describe nearly 98% of the variance in the full data set, and they are all that are used in the parameterization. Excluding the higher-order EOFs not only reduces the size of the data set, but also removes much of the noise from it.

[72] Now, rather than parameterizing R as a function of $\theta_\circ$, λ (or α), θ_v, and ϕ, we separately parameterize the values in the first and second columns of **V** (we refer to these values as v_1 and v_2) as functions of $\theta_\circ$ and, in this case, λ. These coefficients can be represented with fairly simple functions. The form of these functions and the method used to optimize them is discussed below. Figure 10 shows the results of the parameterization of v_1 for this example. Figure 10 (top) shows contours of the actual coefficients matching the measured R-patterns, smoothed with running means in both dimensions, and the results of the parameterization for these coefficients are contoured on the bottom. The parameterizations were fit to the unsmoothed coefficients.

[73] Now, v_1 and v_2 can be calculated for any wavelength and solar zenith angle in the valid range for this parameterization. Once they are calculated, they can be used to calculate the values of R at the 288 grid points by using equation (6), in which **U** is now a 288×2 matrix, with the first two previously determined EOFs in its columns, **Σ** is a 2×2 matrix, with the first two previously determined scale factors on its diagonal, and **V** is the 1×2 matrix, $[v_1\ v_2]$. If the user calculates v_1 and v_2 for multiple combinations of $\theta_\circ$ and λ, multiple patterns of R can be calculated by adding more rows to the matrix **V**. For an arbitrary viewing angle within the defined limits but not on the grid, one must determine R by interpolation.

[74] This process was repeated for each of the six groups of data to be parameterized. The number of EOFs retained was decided by considering three factors: the amount of variance each EOF described, the form of each EOF (an EOF that does not show some reasonable structure is likely representing noise), and the variability of the coefficients in **V** for each EOF with $\theta_\circ$ and λ or α (if the coefficients do not show a systematic variation with at least one of the independent variables then it is likely that the EOF is

representing noise). No hard rules were used to determine the cut off, but the appropriate number was generally obvious on the basis of the above criteria. If there was any doubt about whether to include another EOF, the decision was made on the basis of whether its inclusion improved the results. The first two EOFs were used (and,
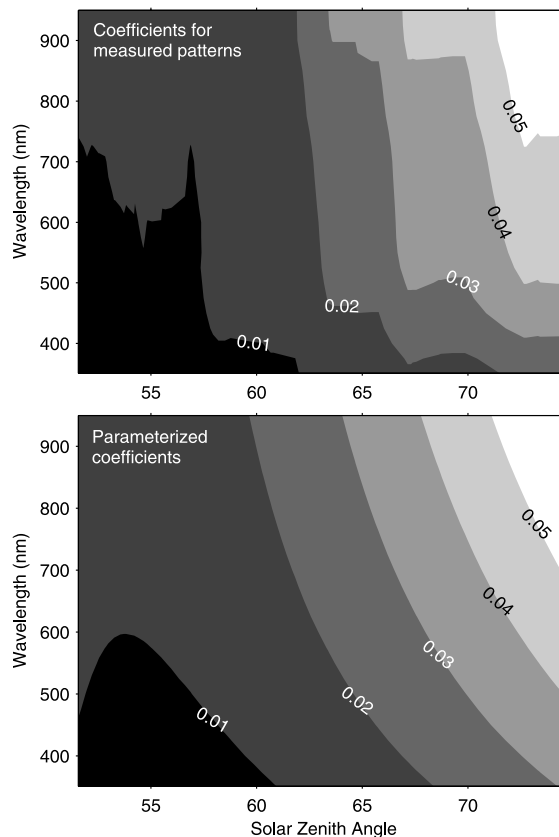
Figure 10. Contour plots of the coefficients multiplying the first EOF of the data in parameterization A. (top) Coefficients fitting the measured data, smoothed with 2.5° and 50-nm running means. (bottom) Parameterized coefficients.

Table 2. Equations for the Coefficients in $\mathbf{V}$ and the Scaling Factors in $\mathbf{\Sigma}$ for Each Parameterization[a]

Parameterization	Equation for v_x	Value of $\Sigma_{x,x}$
A	$v_1 = -0.0258 + 1.34\mu_\circ^{10.1} + 0.181\lambda^{0.519} - 0.206(\mu_\circ\lambda)^{0.608}$	75.6
A	$v_2 = 0.105 - 0.0365\mu_\circ^{-1.01} - 0.00730\lambda^{-1.63} + 4.94 \times 10^{-5}(\mu_\circ\lambda)^{-2.86}$	24.2
B	$v_1 = -0.784 + 1.35\mu_\circ^{-0.0872} - 0.399\lambda^{0.251} - 0.213(\mu_\circ\lambda)^{-0.284}$	217
B	$v_2 = 1.90 + 1.39\mu_\circ^{1.32} - 0.0671\lambda^{-1.11} - 2.43(\mu_\circ\lambda)^{0.101}$	17.9
C	$v_1 = -0.0623 - 7.98 \times 10^{-5}\alpha^{-5.99} + 0.0519(\mu_\circ\alpha)^{-0.454}$	121
C	$v_2 = 0.0902 - 0.0349\mu_\circ^{-1.07}$	23.9
D	$v_1 = -0.195 - 0.000372\mu_\circ^{-1.67} + 0.0569\alpha^{0.369} + 0.118(\mu_\circ\alpha)^{-0.216}$	289
D	$v_2 = 1.75 - 0.132\mu_\circ^{-0.592} + 0.179\alpha^{3.11} - 1.91(\mu_\circ\alpha)^{0.146}$	21.8
D	$v_3 = 0.644 + 1.92\mu_\circ^{1.12} - 0.0221\alpha^{-2.82} - 1.61(\mu_\circ\alpha)^{0.298}$	16.8
E	$v_1 = 0.106 - 0.124(\mu_\circ\alpha)^{0.193}$	129
F	$v_1 = 0.0161 - 0.0103(\mu_\circ\alpha)^{-0.599}$	301
F	$v_2 = -0.151 + 0.0850\mu_\circ^{-0.679}$	36.8

[a]Note that $\mu_\circ \equiv \cos\theta_\circ$ and λ is in μm.

therefore, v_1 and v_2 were parameterized) for parameterizations A, B, C, and F (see Table 1 for definitions of these labels). Parameterization D required the first three EOFs, while parameterization E required only the first EOF. In all cases the EOFs that were retained describe more than 97% of the variance in the data set. All 12 EOFs that are used in these parameterizations are available as delimited ASCII files with the auxiliary material published online with this paper and available on our website: http://www.atmos.washington.edu/~sgwgroup/DC/brdfPaper.html.

[75] For each parameterization, the necessary values in $\mathbf{\Sigma}$ and the equations to calculate the necessary elements of $\mathbf{V}$ are presented in Table 2. After looking at contour plots of the coefficients in $\mathbf{V}$ for the various groups of data, we decided on the following functional form for the parameterization of those values:

$$v = c_1 + c_2\mu_\circ^{c_3} + c_4\lambda^{c_5} + c_6(\mu_\circ\lambda)^{c_7}, \qquad (7)$$

where $\mu_\circ \equiv \cos(\theta_\circ)$. The function nlinfit, part of Matlab's Statistics Toolbox, was used to find the optimum values of c_i in a least-squares sense. This optimization was also attempted while leaving out various terms in equation (7), and only those terms in the equations that improved the results were retained. Therefore the exact form of the equations shown in Table 2 varies.

4.2.3. Parameterization Results

[76] The last two columns of Table 1 show the root-mean-squared relative error (RMSE) for each of the parameterizations. When possible, two RMSEs are given, one for the entire parameterization, and another calculated only for $\theta_v \leq 52.5°$, which are the viewing angles most likely to be used for remote sensing. The errors shown in Table 1 are in line with the estimated uncertainties in the data, discussed in section 3.4. The magnitude of the error does not vary significantly across each parameterization's valid range of solar zenith angles or wavelengths.

[77] Figure 11 shows the calculated values of R corresponding to the five observations shown in Figure 3 that are covered by the parameterizations. The plots on the right side of Figure 11 were created by combining the two parameterizations for long wavelengths. Comparing the plots in Figure 11 to those in Figure 3 shows that the

parameterizations accurately represent the main features seen in the data.

[78] The errors in Figure 11, relative to the data in Figure 3, are shown in Figure 12. These plots show that the largest errors are often found at large viewing zenith angles, especially in the forward scattering direction.

[79] No normalization requirement was placed on the parameterization results, so the patterns they predict do not necessarily satisfy equation (2). This deviation from the correct normalization will introduce a small error when converting radiance measurements to albedo. For the parameterized patterns, the left hand side of equation (2) is between 0.993 and 1.01 for parameterizations A and B, 0.996 and 1.005 for parameterizations C and D, and 0.985 and 1.02 for the combination of parameterizations E and F.

4.2.4. Parameterization Uncertainties

[80] In section 3.4 we considered factors that could introduce errors and noise into any of our individual analyzed reflectance patterns. Here we consider factors that may lead to variation in the reflectance pattern of the snow surface between our observations, and discuss how they might affect the parameterizations.

[81] Of the five factors listed in section 3.4 that affect the BRDF of snow, the parameterizations account for one directly and a second indirectly. The solar zenith angle is one of the independent variables in our parameterizations. The second independent variable is wavelength or albedo; this second independent variable accounts for variations in the absorption coefficient of ice, among other things. The other factors given above are not directly accounted for in our parameterizations and will introduce some level of uncertainty.

[82] Grain size variations during the two summers are a possible source of uncertainty in the parameterization. An increase in grain size primarily affects the BRDF of snow through two mechanisms: the asymmetry parameter (g) is increased [*Wiscombe and Warren*, 1980], and the path length through ice between scattering events at air-ice interfaces is increased. Both of these effects increase the anisotropy of the BRDF pattern, strengthening the forward reflectance peak of the snow. Frequent observations of the surface snow showed that it was composed of grains with approximate radii between 50 and 100 μm, and that the range of sizes did not vary much during the field seasons.
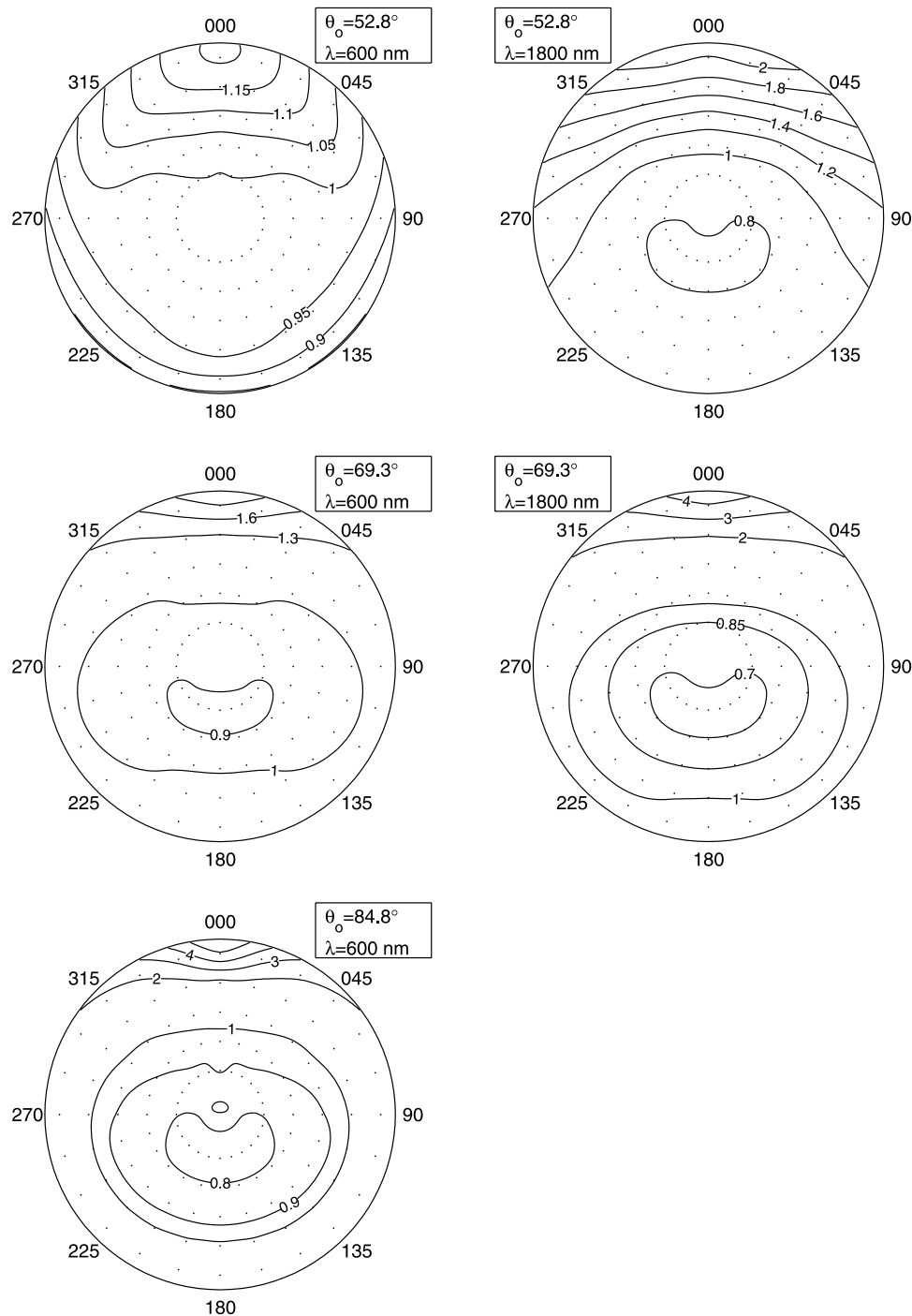
Figure 11. Polar contour plots of R, calculated with the parameterizations for five of the six observations shown in Figure 3. The sixth observation in Figure 3 is not covered by any of our parameterizations. The contour interval sometimes changes at 1.

This size range is typical of the Antarctic Plateau, and the small magnitude of the variations minimizes the uncertainty they cause. Measurements of spectral albedo made on two traverses from Dome C to the coast at 67°S showed that the effective grain size was constant from latitude 75°S (Dome C) to latitude 68°S (R. E. Brandt and S. G. Warren, manuscript in preparation, 2006).

[83] Variations in the single-scattering phase function of the snow grains can be examined by looking at variations in g. As mentioned above, g increases with grain size; it is also a function of wavelength. Its dependence on wavelength will be accounted for in the parameterizations through their dependence on wavelength and albedo. Its variation with grain size will introduce uncertainty into our parameterizations because we do not account for grain size variations. This uncertainty will be small at wavelengths shorter than 1000 nm, where g varies little with grain size [*Wiscombe and Warren*, 1980, Figure 4], but may be more
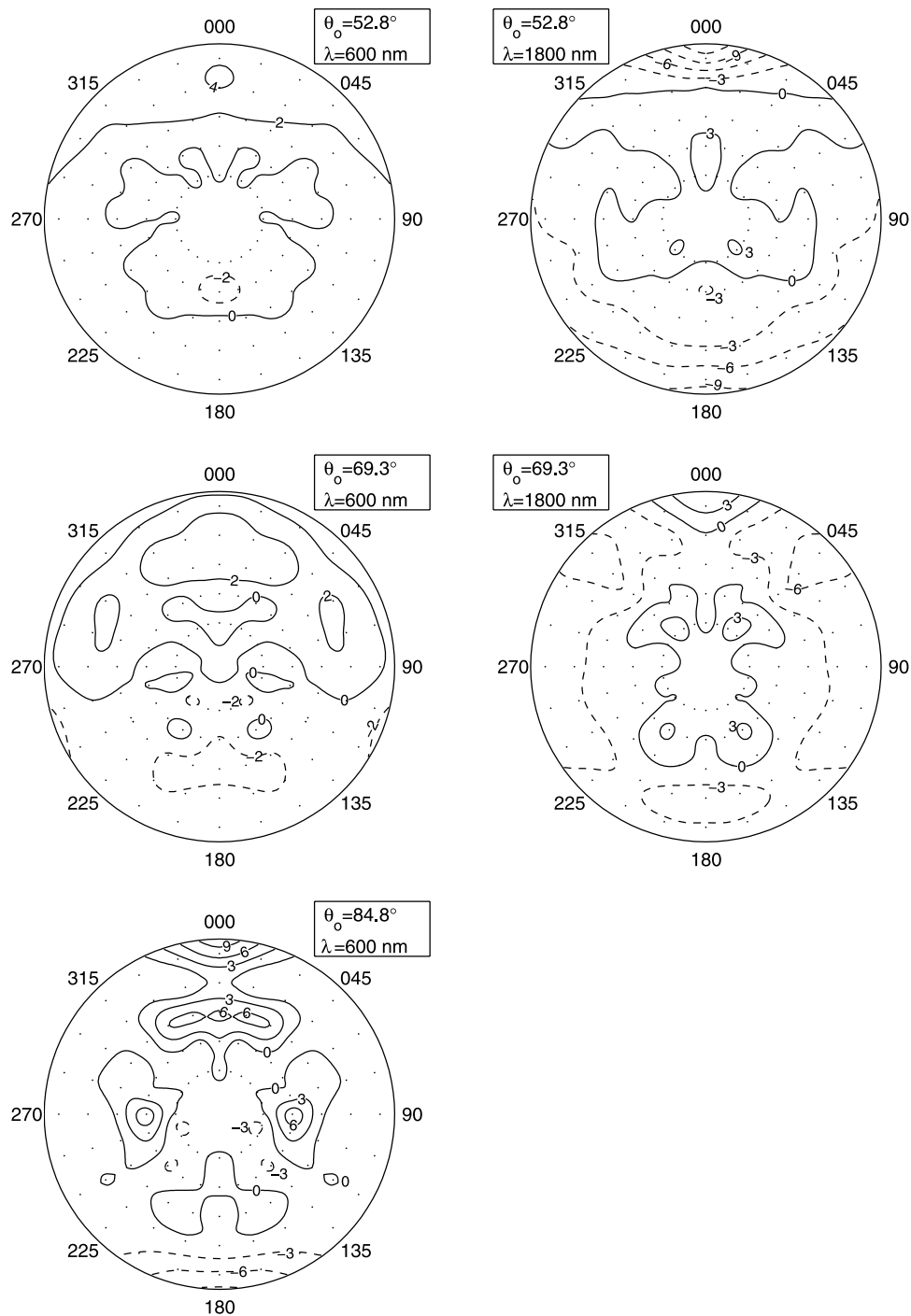
Figure 12. Polar contour plots of the relative error (%) of R, calculated with the parameterizations for five of the six observations shown in Figure 3. The sixth observation in Figure 3 is not covered by any of our parameterizations. Contours of negative values are dashed and indicate angles at which the parameterized R is less than the observed R.

significant at longer wavelengths. Since modeling the BRDF of the snow surface with plane-parallel radiative transfer models does not match measurements for the natural rough surface, as discussed below in section 5.2, it is difficult to quantitatively assess the variability of R that results from the small grain size variations that occurred between our observations. However, it seems likely that much of the variation between observations made on

different days at similar solar zenith angles (discussed at the end of section 3.4) is due to these grain size variations.

[84] Our parameterizations also contain some level of uncertainty due to changes in the dimensions and orientation of the surface roughness features in the two summers during which we collected the data. It is only the variability of the features that introduces uncertainty into our parameterization, and while the exact shape and location of
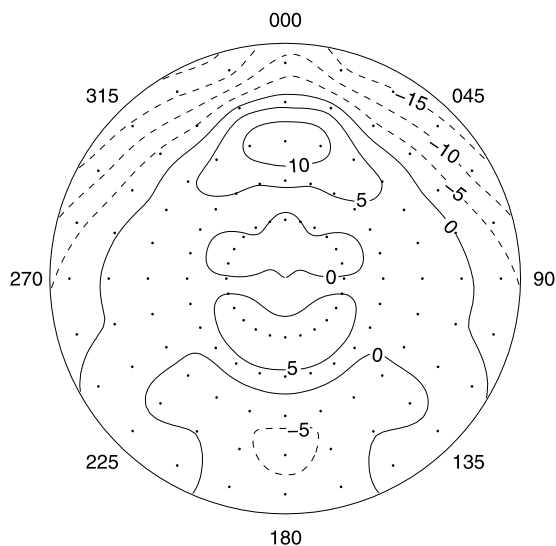
Figure 13. Relative difference (%) between observations of R at 900 nm from South Pole and Dome C. Negative contours are dashed and indicate angles at which R was greater at Dome C than at South Pole. The solar zenith angle at the time of the observations was 73.3° at Dome C and 73.5° at South Pole. The South Pole data are from Figure 4b of *Warren et al.* [1998].

particular features changed over time, the overall character of the surface roughness did not change noticeably. Therefore, given that our measurement footprints were large enough, these changes will have little effect on the parameterizations.

[85] Ultimately the parameterizations ignore much of the minor variability caused by day-to-day changes, and focus on the most significant ways in which the BRDF varies with solar zenith angle and either wavelength or albedo. This produces parameterizations valid for "average" conditions on the high parts of the Antarctic Plateau. The RMSE (Table 1) of the parameterizations provides some quantitative estimates of the uncertainty in the parameterizations.

5. Discussion

5.1. Comparison of Dome C to South Pole

[86] The parameterizations presented above may apply only to the snow at Dome C since all of the data were collected there. However, we suggest that they can also be applied to snow on other high parts of the plateau, where surface features are similar to those at Dome C. Here we investigate whether they can be applied to areas of the plateau away from the domes and ridges by looking at a comparison with data from the South Pole.

[87] Figure 13 shows the relative difference between two observations of R at $\lambda = 900$ nm, one made at Dome C with $\theta_\circ = 73.3°$ and the other made at the South Pole with $\theta_\circ = 73.5°$; the South Pole data were presented in Figure 4b of *Warren et al.* [1998]. The differences at most angles are less than 10%. Given the uncertainties in both observations, this comparison suggests the data from Dome C are representative of conditions on other parts of the plateau, except at large viewing zenith angles in the forward scattering direction, the region most affected by sastrugi.

[88] A similar comparison between the South Pole observation and the parameterization results at $\lambda = 900$ nm and $\theta_\circ = 73.5°$ (not shown) also indicated differences less than 10% at viewing zenith angles less than about 55°, but larger differences at larger viewing zenith angles, especially in the backscatter direction. Taking these two examples together, along with results from *Warren et al.* [1998] showing that the effect of sastrugi was mostly limited to large θ_v, we suggest the parameterizations may be applied to areas of the Antarctic Plateau with large-scale surface slope similar to that at the South Pole at viewing zenith angles less than 55°.

5.2. Comparison of Rough and Flat Surfaces

[89] We have referred to the effect of sastrugi and surface roughness on the BRDF of snow but we have not been able to show exactly what effect these features have. Figure 14 shows the observed pattern of reflectance at $\lambda = 900$ nm and $\theta_\circ = 64.8°$ along with the reflectance predicted by DISORT, a multiple-scattering radiative-transfer model [*Stamnes et al.*, 1988], for the same wavelength and solar zenith angle. The snow in DISORT was described as a semi-infinite layer with particle effective radii of 100 μm (the single-scattering albedo and asymmetry parameter were calculated with Mie theory for 100-μm ice spheres, and their phase function was then specified as the Henyey-Greenstein phase function with the asymmetry parameter determined from Mie theory).

[90] This modeled snow surface is perfectly flat, so the reflectance pattern shown in Figure 14b should be representative of that from a snow surface with no surface roughness. These two patterns together suggest that the surface roughness greatly reduces the forward reflectance peak (because an observer looking toward the sun sees shaded surfaces) and enhances the backward reflectance (because the roughness effectively reduces the incident zenith angle on roughness elements viewed when looking away from the sun). These effects of the surface roughness, combined with the tendency of the reflectance from a smooth snow surface to decrease continuously from forward to backward scattering angles, results in the observed minimum values of R, located at small viewing zenith angles in the backscattered direction.

[91] The phase function of the real snow grains differs from the Henyey-Greenstein phase function, so some of the differences between Figures 14a and 14b could be due to an inadequate specification of the phase function in the model. Similar modeling in the future, using a variety of realistic phase functions, will further illustrate the degree to which this difference is caused by surface roughness. *Leroux and Fily* [1998] modeled the effect of sastrugi on the BRDF of snow and found that they do significantly reduce the forward reflectance while enhancing the backward reflectance. Their results support the suggestion that much of the difference between the measured and modeled reflectance in Figure 14 is due to the presence of sastrugi on the Dome C snow surface.

5.3. Is BRDF Constant Across the Visible and Near-UV?

[92] As discussed in section 2, the values of R presented here for wavelengths less than about 800 nm are not directly related to the true BRDF of the snow because of the
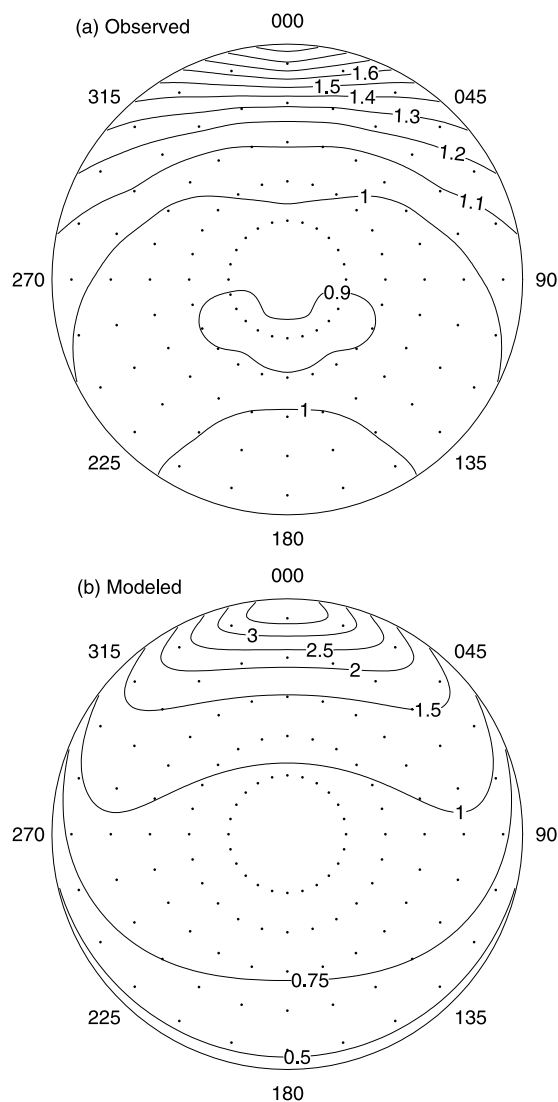
Figure 14. Values of R at 900 nm, $\theta_\circ = 64.8°$, (a) observed for the natural rough surface at Dome C and (b) modeled for a hypothetical flat surface with DISORT.

significant amount of diffuse light reaching the surface at wavelengths where Rayleigh scattering is effective. Often the user of these parameterizations may wish to obtain the true BRDF at these wavelengths, and here we discuss a method that may provide this.

[93] We have seen that at wavelengths where Rayleigh scattering is not important, and at which R is therefore directly related to the true BRDF by equation (5), R varies smoothly with α. Furthermore, extrapolating the relationship seen in Figure 7 at $\alpha < 0.9$ (wavelengths where Rayleigh scattering is not important) to $\alpha = 1.0$ suggests that, were there no diffuse light at these wavelengths, R would not vary much between $\alpha = 0.9$ and $\alpha = 1.0$. On the basis of these observations, it might be reasonable to assume that the BRDF at any wavelength at which Rayleigh scattering affects our observations can be determined from our observed values of R at 800 or 900 nm, where α is around 0.9 and Rayleigh scattering is unimportant.

[94] To test this idea in the near-UV where Rayleigh scattering is very strong, we again made use of DISORT, this time applied to the atmosphere rather than the snow. Figure 14 shows that simple implementations of DISORT cannot accurately model the reflectance from the snow surface, so we instead specified the surface BRDF at $\lambda = 375$ nm to be the same as that measured at 900 nm (but accounting for the difference in albedo)

$$\rho(\lambda = 375 \text{ nm}, \theta_\circ = 64.8°, \theta_v, \phi)$$
$$= \frac{\alpha(\lambda = 375 \text{ nm})}{\pi} R(\lambda = 900 \text{ nm}, \theta_\circ = 64.8°, \theta_v, \phi).$$

This form comes from equation (5), with the assumption that $R(\lambda = 375 \text{ nm})$ would equal $R(\lambda = 900 \text{ nm})$ if there were no diffuse light. We then used DISORT to apply the direct and diffuse downwelling radiation fields at 375 nm to the surface based on $R(\lambda = 900 \text{ nm})$, and compare the predicted upwelling radiation to the parameterization of $R(\lambda = 375 \text{ nm})$.

[95] If our assumption is true that without diffuse light R would be similar at all wavelengths less than 900 nm, then the radiance reflected from the surface in this model should produce a pattern similar to our parameterization of R for $\lambda = 375$ nm and $\theta_\circ = 64.8°$. Figure 15 shows the relative difference between the two. The model produced slightly too much forward reflectance, but agrees with the parameterization to within 4% at most angles and to within 7% everywhere, supporting our assumption. One possible cause for the differences shown in Figure 15 is the exclusion of aerosols and boundary layer ice crystals from our model atmosphere; these would create more diffuse light, which would decrease the forward reflectance peak and increase reflectance elsewhere.

[96] The BRDF of the lower boundary in DISORT must be specified for all incidence angles from the sky-hemisphere, but our parameterizations are valid only for a limited range of incidence angles. We assumed an isotropic BRDF for an incidence angle of 0°, and specified the BRDF for incidence angles less than 51.6° as a linear interpolation between the isotropic pattern and that predicted for an incidence angle of 51.6°. While this is not likely to be completely accurate, the errors resulting from this approximation should be small since the BRDF at 51.6° is already nearly isotropic. The BRDF at incidence angles greater than 86.6° was specified as being equal to that at 86.6°.

[97] For DISORT to determine the downwelling radiance field at the surface, it requires as input the optical depth, single-scattering albedo, and phase function of layers above the surface that represent the effect of the Dome C atmosphere on 375-nm light. The properties of these "atmospheric" layers were determined by using SBDART [*Ricchiazzi et al.*, 1998], a spectral atmospheric radiative transfer model developed around DISORT, which uses spectral transmission data to determine the radiative properties of atmospheric layers given vertical profiles of temperature, pressure, water vapor, and ozone, along with aerosol data. SBDART was run with an atmospheric profile that was typical of the summertime atmosphere at Dome C. The output from SBDART included the optical depth and single-scattering albedo for the atmospheric layers, which

Figure 15. Relative difference (%) between parameterized values of R at 375 nm, $\theta_\circ = 64.8°$ and modeled values of R, computed with DISORT by placing layers representative of a typical Dome C summertime atmosphere, with properties appropriate for 375 nm, above a surface with a BRDF specified as equal to the parameterization at 900 nm with $\theta_\circ = 64.8°$. Negative contours are dashed and indicate angles at which the DISORT results were less than the parameterization.

we then used, with the Rayleigh phase function, as the atmospheric layers in DISORT. DISORT could then be used to model the radiative transfer from the top of the atmosphere to just after interaction with the surface. SBDART was used only to generate the appropriate input for DISORT because SBDART does not allow for the specification of an arbitrary lower BRDF.

[98] In the atmospheric profile used as input to SBDART, temperature, pressure, and water vapor concentration below 28 km were specified as the mean of 47 radiosoundings conducted at Dome C during January 2004. Ozone concentration at all heights, and all quantities above 28 km were taken from the summertime South Pole model atmosphere of *Walden et al.* [1998], who used ozonesonde data for ozone concentrations below 30 km, and various satellite data for all quantities above 30 km. Our model atmosphere did not include any aerosols.

6. Summary

[99] The data presented in this paper were collected at a high part of the Antarctic Plateau, where the surface slope is extremely small. As a result of the small slope, the winds at this site are both less intense and less directionally constant, resulting in a smoother and more randomized snow surface, than at other Antarctic locations at which the surface BRDF has previously been studied. The smoother snow surface minimizes the effect of the varying azimuth angle between the sun and the dominant direction of orientation of the surface roughness features, eliminating one of the difficulties that various remote sensing techniques must handle on the plateau.

[100] The advantages of this location, combined with newer spectroscopic technology, allowed us to collect enough data during two summers to produce parameterizations that predict the anisotropic reflectance factor of the snow in this region, for most of the solar spectrum and for a wide range of solar zenith angles, with a high degree of accuracy. The development of relatively simple parameterizations was made possible by using the empirical orthogonal functions of the data set as our basis functions. Here we discuss some of the issues that must be considered when using these parameterizations.

[101] Since the data were collected in just one location, the parameterizations are not necessarily applicable to the entire continent, nor to any other snow surfaces away from Dome C. However, with proper consideration, they can be used for some other areas. Most immediately, any part of the high Antarctic Plateau with small surface slope is likely to have similar surface properties to the area around Dome C, meaning these can probably be used around Dome A and along the ridge between Domes A and C with a good deal of confidence. Most other areas of the plateau have larger slopes and therefore larger sastrugi. *Warren et al.* [1998] showed that the sastrugi at South Pole caused very little variation of the BRDF at viewing zenith angles less than about 50°. A comparison of data from Dome C and South Pole show that the data do not differ much at viewing zenith angles less than about 55°. For these reasons, the parameterizations should produce reasonable estimates of the anisotropic reflectance factor for any part of the Antarctic Plateau with sastrugi not much larger than those found at South Pole, as long as their use is limited to $\theta_v \lesssim 55°$. Perhaps they can also be applied, with caution, to the highest parts of the Greenland Ice Cap, in areas that do not experience melting.

[102] The parameterizations should not be applied to the slope between the plateau and the coast of Antarctica. Winds in those areas tend to be both strong and directionally constant, resulting in large and well-aligned sastrugi, which may affect the reflectance even into near-nadir angles.

[103] Snow in midlatitudes and seasonal Arctic snow may differ from snow on the Antarctic Plateau in any of several ways: it may not have significant macroscale surface roughness, it may contain more soot and other natural or anthropogenic contamination, it usually forms at higher temperatures thus producing larger snow grains, it experiences melting and more rapid metamorphism, and it may be affected by vegetation. Any of these factors would cause the BRDF to differ from these parameterizations.

[104] In using these parameterizations, there are a few things to consider. Each parameterization was developed with a certain set of data, and none should be used outside of the range of parameters that is covered by its data set (shown in Table 1).

[105] Parameterizations C–F were developed using the measured values of spectral albedo of the snow at Dome C (Figure 6) as a predictor of R, rather than wavelength; this made more physical sense in these spectral regions than using wavelength directly. Perhaps, when applying these parameterizations, the user can estimate the albedo of the snow of interest, and can use that directly (doing so should help to compensate for grain size differences between the snow of interest and the snow at Dome C). This idea has not been tested, and so should be used cautiously; if the

expected albedo at a given wavelength is outside the range of albedos used to develop the parameterizations then it is unlikely that they will work for the snow of interest. If the user does not have a better estimate of albedo, then the values presented here for the development of the parameterizations (Figure 6, and in tabular form with the online auxiliary material) may be used.

[106] Users should be cautious when applying the parameterizations to the visible and ultraviolet region of the spectrum since the predicted value of R at these wavelengths is not directly related by equation (5) to the true BRDF because of the significant amount of diffuse incident light. If the true BRDF is the desired result in this spectral region, it can be determined from equation (5) by using $R(\lambda = 900$ nm$)$ and the albedo at the wavelength of interest.

[107] The parameterizations presented here are, to the authors' knowledge, the most comprehensive set available that are based on data. The difficulties of accurately modeling the angular reflectance of snow are many, and it is a time-consuming process, especially correctly accounting for surface roughness. We hope that these parameterizations will reduce the need for this modeling, and provide points for comparison when such modeling is necessary or desired. Our parameterizations can also provide good lower boundary conditions for atmospheric radiative transfer modeling over snow, allowing for estimates of the top-of-atmosphere BRDF for use with satellite data.

References

Aoki, T., T. Aoki, M. Fukabori, A. Hachikubo, Y. Tachibana, and F. Nishio (2000), Effects of snow physical parameters on spectral albedo and bidirectional reflectance of snow surface, *J. Geophys. Res.*, *105*(D8), 10,219–10,236.

Arnold, G. T., S.-C. Tsay, M. D. King, J. Y. Li, and P. F. Soulen (2002), Airborne spectral measurements of surface-atmosphere anisotropy for arctic sea ice and tundra, *Int. J. Remote Sens.*, *23*(18), 3763–3781, doi:10.1080/01431160110117373.

Grenfell, T. C., S. G. Warren, and P. C. Mullen (1994), Reflection of solar radiation by the Antarctic snow surface at ultraviolet, visible, and near-infrared wavelengths, *J. Geophys. Res.*, *99*(D9), 18,669–18,684.

Kindel, B. C., Z. Qu, and A. F. H. Goetz (2001), Direct solar spectral irradiance and transmittance measurements from 350 to 2500 nm, *Appl. Opt.*, *40*(21), 3483–3494.

Kokhanovsky, A. A., T. Aoki, A. Hachikubo, M. Hori, and E. P. Zege (2005), Reflective properties of natural snow: Approximate asymptotic

theory versus in situ measurements, *IEEE Trans. Geosci. Remote Sens.*, *43*(7), 1529–1535, doi:10.1109/TGRS.2005.848414.

Kuhn, M. (1985), Bidirectional reflectance of polar and alpine snow surfaces, *Ann. Glaciol.*, *6*, 164–167.

Leroux, C., and M. Fily (1998), Modeling the effect of sastrugi on snow reflectance, *J. Geophys. Res.*, *103*(E11), 25,779–25,788.

Leroux, C., J.-L. Deuzé, P. Goloub, C. Sergent, and M. Fily (1998), Ground measurements of the polarized bidirectional reflectance of snow in the near-infrared spectral domain: Comparisons with model results, *J. Geophys. Res.*, *103*(D16), 19,721–19,731.

Li, S., and X. Zhou (2004), Modelling and measuring the spectral bidirectional reflectance factor of snow-covered sea ice: An intercomparison study, *Hydrol. Processes*, *18*(18), 3559–3581, doi:10.1002/hyp.5805.

Loeb, N. G. (1997), In-flight calibration of NOAA AVHRR visible and near-IR bands over Greenland and Antarctica, *Int. J. Remote Sens.*, *18*(3), 477–490, doi:10.1080/014311697218908.

Loeb, N. G., S. Kato, K. Loukachine, and N. Manalo-Smith (2005), Angular distribution models for top-of-atmosphere radiative flux estimation from the Clouds and the Earth's Radiant Energy System instrument on the Terra satellite. Part I: Methodology, *J. Atmos. Oceanic Technol.*, *22*, 338–351, doi:10.1175/JTECH1712.1.

Masonis, S. J., and S. G. Warren (2001), Gain of the AVHRR visible channel as tracked using bidirectional reflectance of Antarctic and Greenland snow, *Int. J. Remote Sens.*, *22*(8), 1495–1520, doi:10.1080/01431160121039.

Michalsky, J. J. (1988), The Astronomical Almanac's algorithm for approximate solar position (1950–2050), *Sol. Energy*, *40*(3), 227–235, doi:10.1016/0038-092X(88)90045-X.

Nicodemus, F. E., J. C. Richmond, J. J. Hsia, I. W. Ginsberg, and T. Limperis (1977), *Geometrical Considerations and Nomenclature for Reflectance*, NBS Monogr., vol. 160, Natl. Inst. of Stand. and Technol., Gaithersburg, Md.

Painter, T. H., and J. Dozier (2004), Measurements of the hemispherical-directional reflectance of snow at fine spectral and angular resolution, *J. Geophys. Res.*, *109*, D18115, doi:10.1029/2003JD004458.

Ricchiazzi, P., S. Yang, C. Gautier, and D. Sowle (1998), SBDART: A research and teaching software tool for plane-parallel radiative transfer in the Earth's atmosphere, *Bull. Am. Meteorol. Soc.*, *79*(10), 2101–2114, doi:10.1175/1520-0477(1998)079<2101:SARATS>2.0.CO;2.

Stamnes, K., S.-C. Tsay, W. Wiscombe, and K. Jayaweera (1988), Numerically stable algorithm for discrete-ordinate-method radiative transfer in multiple scattering and emitting layered media, *Appl. Opt.*, *27*(12), 2502–2509.

Suttles, J. T., et al. (1988), *Angular Radiation Models for Earth-Atmosphere System*, vol. 1, *Shortwave Radiation*, NASA Ref. Publ. 1184.

Walden, V. P., S. G. Warren, and F. J. Murcray (1998), Measurements of the downward longwave radiation spectrum over the Antarctic Plateau and comparisons with a line-by-line radiative transfer model for clear skies, *J. Geophys. Res.*, *103*(D4), 3825–3846.

Warren, S. G., and A. D. Clarke (1990), Soot in the atmosphere and snow surface of Antarctica, *J. Geophys. Res.*, *95*(D2), 1811–1816.

Warren, S. G., R. E. Brandt, and P. O'Rawe Hinton (1998), Effect of surface roughness on bidirectional reflectance of Antarctic snow, *J. Geophys. Res.*, *103*(E11), 25,789–25,807.

Warren, S. G., R. E. Brandt, and T. C. Grenfell (2006), Visible and near-ultraviolet absorption spectrum of ice from transmission of solar radiation into snow, *Appl. Opt.*, *45*, 5320–5334, doi:10.1364/AO.45.005320.

Wiscombe, W. J., and S. G. Warren (1980), A model for the spectral albedo of snow. I: Pure snow, *J. Atmos. Sci.*, *37*(12), 2712–2733, doi:10.1175/1520-0469(1980)037<2712: AMFTSA>2.0.CO;2.

————————————

R. E. Brandt, T. C. Grenfell, S. R. Hudson, and S. G. Warren, Department of Atmospheric Sciences, University of Washington, Box 351640, Seattle, WA 98195-1640, USA. (brandt@atmos.washington.edu; tcg@atmos.washington.edu; hudson@atmos.washington.edu; sgw@atmos.washington.edu)

D. Six, Laboratoire de Glaciologie et Géophysique de l'Environnement, CNRS/UJF, 54 rue Molière, BP 96, F-38402 Saint Martin d'Hères Cedex, France. (six@lgge.obs.ujf-grenoble.fr)